Advanced core characterisation to improve multiphase flow prediction in heterogeneous sandstone and carbonate rocks

Nele Wenck[1], *Samuel* Jackson[2,1], *Ann* Muggeridge[1], *and Samuel* Krevor[1]

[1]Department of Earth Science and Engineering, Imperial College London, United Kingdom
[2]CSIRO Energy, Private Bag 10, Clayton South, Victoria 3169, Australia

Abstract Characterisation of multiphase flow properties is crucial in predicting large-scale fluid behaviour in the subsurface, for example CO_2 plume migration at CCS storage sites. One gap in conventional reservoir simulation workflows is the field scale representation of the impact of small-scale capillary heterogeneities. We present an approach to characterising rock samples, which combines core flood experimental data with a numerical optimisation scheme, developed by Jackson et al. (2018). We apply the characterisation effort to a carbonate and two sandstone cores with distinct types and length scales of heterogeneities. The Bentheimer and Bunter sandstones exhibit parallel and perpendicular layering, respectively, whereas the Edwards Brown dolomite is characterised by isotropic, multi centimetre cementation. We use the digital core models to predict the relative permeability of both phases at distinct flow rates. The isotropic heterogeneity in the Edwards Brown dolomite resulted in non-monotonic behaviour as the flow rate was reduced; initially the gas relative permeability increases, and subsequently decreases with approach to the capillary-limit. This work highlights the significant contrast in fluid behaviour between sandstones and carbonates caused by variations in capillary characteristics and underscores the importance of characterising these small-scale heterogeneities for field studies.

1 Introduction

1.1 Introduction to multiphase flow properties

The characterisation of multiphase flow properties is crucial in predicting large-scale fluid flow behaviour, for example for the prediction of plume migration at carbon capture and storage (CCS) injection sites or in field development plans for hydrocarbon production. Subsurface fluid flow is governed by the multiphase Darcy law [1,2]:

$$q_p = \frac{-Kk_{rp}}{\mu_p}(\Delta P_p - \rho_p g) \qquad 1$$

where q is the Darcy velocity (ms^{-1}), K is the permeability (m^2), μ is the viscosity (Pa s), P is the pressure (Pa), ρ is the density (kgm^{-3}) and g is gravity acceleration (ms^{-2}). k_{rp} is the relative permeability of phase p and the subscript p refers to the property of a phase. Relative permeability is one of the key parameters controlling fluid behaviour. Historically, flow calculations assumed rocks to be homogeneous, see for example [3]. However, the work from [4] demonstrated that permeability heterogeneity significantly impacts the relative permeability and should thus be incorporated in flow models.

More recently it has become apparent that rocks may be heterogeneous in terms of spatially varying relative permeability and capillary pressure functions. The type and length scale of heterogeneity plays a key role on the observed fluid behaviour [5-7]. For example, layering parallel to flow may result in capillary crossflow, which can be observed as an increase in the phase permeabilities [8].

The ratio of capillary to viscous forces controls the importance of capillary heterogeneity. At the low flow potentials typically encountered in reservoirs, capillary pressure heterogeneity has been shown to significantly alter fluid flow [5-7]. Its importance can be quantified using the capillary number. Throughout this work, we use the definition first proposed by [9] for capillary heterogeneity formed of layers parallel to flow:

$$N_c = \frac{H}{L}\frac{\Delta P}{\Delta P_c} \qquad 2$$

where H [m] is a length scale associated with the heterogeneity, L [m] is the sample length along the flow axis, ΔP [Pa] is the pressure differential across L, and ΔP_c [Pa] is

* Corresponding author: nele.wenck15@imperial.ac.uk

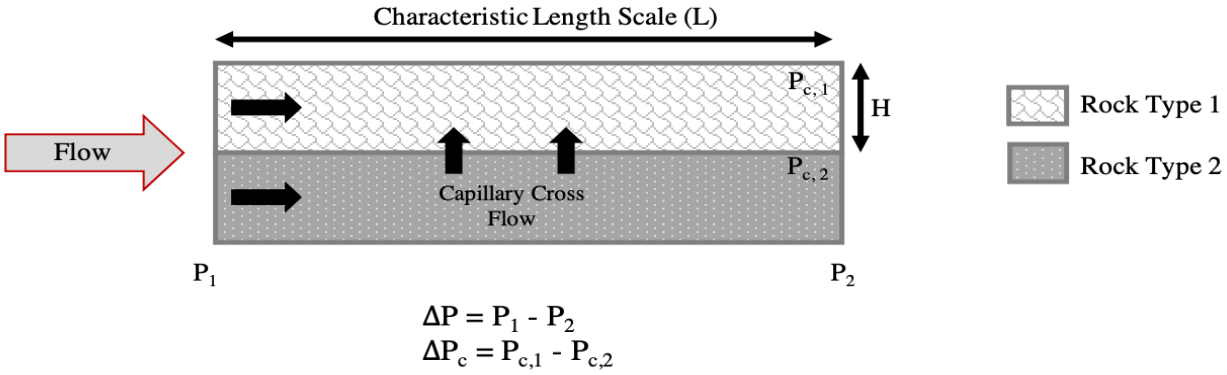

Figure 1: Schematic of layer cross flow arising from capillary heterogeneity in a 2-layer system. The governing parameters from Equation 2 are also depicted.

the contrast in capillary pressure imposed by the heterogeneities (Figure 1).

1.2 Capillary Heterogeneity Characterisation

To model capillary heterogeneity, [10] developed a method, which used capillary pressure and J-function scaling to infer the 3D permeability distribution within a core. The workflow enabled the authors to build a 3D model of the sandstone rock sample, which was verified by comparing experimental and simulation saturation distributions. [11] and [12] built on these results and developed the method further by analysing a wider range of samples. It emerged that gas relative permeability anisotropy was also mainly caused by the presence of capillary heterogeneity within a rock sample.

Even though studies thus far have demonstrated the importance of capillary heterogeneity as one of the dominant fluid distribution mechanisms on a sub-core scale for both brine-oil and brine-gas systems, the established analytical methods used for calculating relative permeability, until recently, failed to incorporate this mechanism. This was the main motivation behind the work of [13]. Two sandstone samples were characterised on a sub-core scale based on the methodology presented in [10]. Thereafter, the authors determined the core-average effective relative permeability using the digital models in a numerical simulation. The work also investigated the factors influencing the rate dependency of relative permeability, which had been observed for many years. They concluded that capillary forces and end effects control this behaviour.

[14] noted that [13] primarily focused on deriving an effective, viscous-limit relative permeability for each sample. This does not describe fluid behaviour at flow rates typically encountered in the subsurface [15]. Instead, fluid flow in these applications is largely in the capillary-limit regime. Hence, the authors proceeded to use the method developed by [13] as a basis to numerically characterise the rock heterogeneity on two samples with differently orientated heterogeneities. Rather than solely deriving the effective relative permeability, the characterisation effort allowed the authors to simulate flow and predict the characteristic relative permeability for a range of capillary numbers (spanning 4 orders of magnitude). Additionally, they removed experimental constraints such as boundary effects.

[16] simultaneously also developed a workflow to characterise heterogeneity in carbonates, but instead, used multi-rate core-flood experiments. The use of multiple rates enabled them to introduce a multi-objective optimization, incorporating both, saturation and pressure. Their goal was to characterise relative drainage capillary pressure curves as well as scaling factors, which quantitatively describe the distribution of heterogeneity within a core. Using three different rock samples, they applied their workflow and presented a close match between simulation and experiment, thereby verifying the method.

1.3 Focus of this study

The aforementioned studies have demonstrated the importance of capillary action as a fluid distribution mechanism. However, the majority of reservoir simulation workflows have thus far failed to incorporate the impact of small-scale heterogeneities on the field scale, leading to incorrect flow predictions, for instance at the Sleipner injection site [17]. This is partly driven by the uncertainty surrounding the characterisation of capillary heterogeneity in reservoir samples and the predicted impact on relative permeability anisotropy. The majority of characterisation studies have focused on well-behaved sandstones. However, reservoirs typically exhibit more complex sedimentary structures.

In this work, we have applied the workflow developed by [14] to three rock samples, two sandstones and one carbonate. The sandstones exhibit distinct planar bedding, one parallel to the axis of flow and one perpendicular to the axis of flow. The carbonate rock is characterised by isotropic heterogeneity - a low-permeable, multi-centimetre, cemented region towards the outlet of the core. Using the methodology, we have produced digital models of the three samples, which incorporate capillary heterogeneity. These models enabled us to predict the relative permeability at a range of flow rates and analyse the varying fluid behaviour in distinct flow regimes.

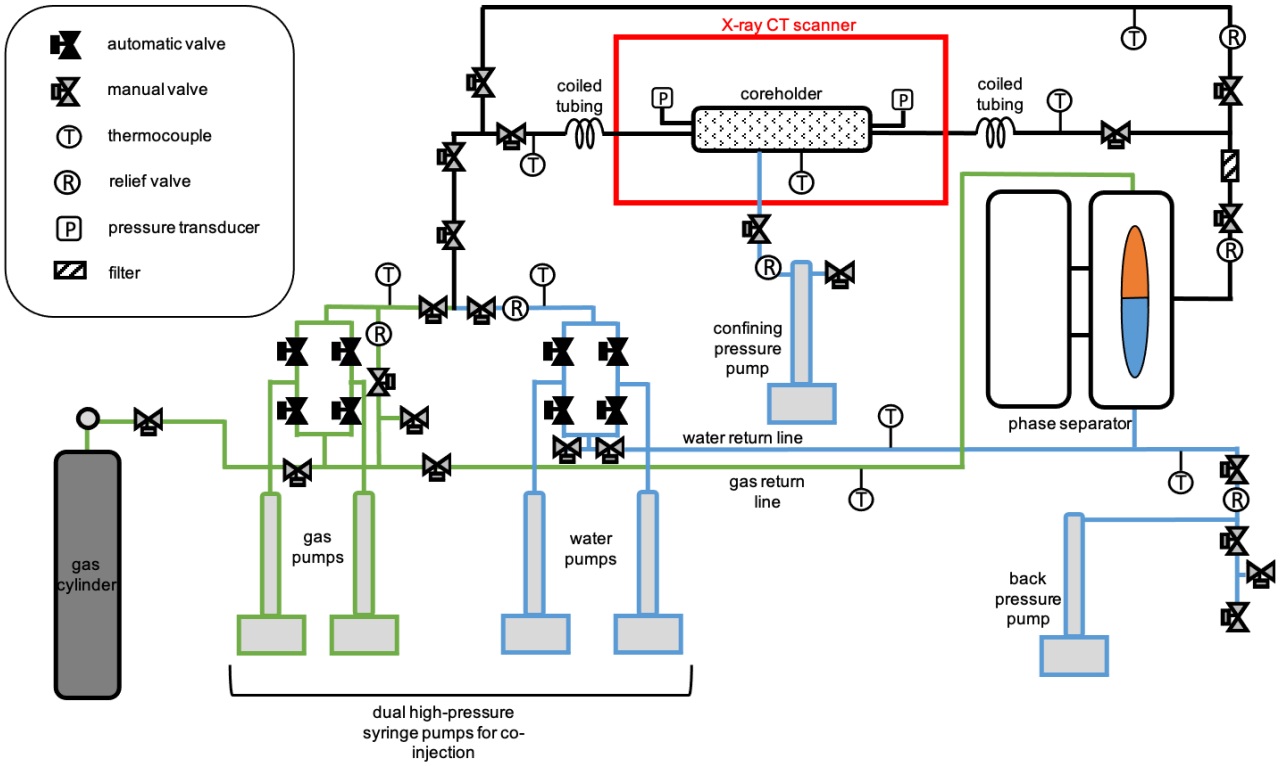

Figure 2: A schematic of the flow loop used for the drainage core flood experiments.

2. Methodology

In this section, we first introduce the rock samples analysed and we then describe the experimental method. This is followed by a detailed description of the numerical modelling, which forms the second part of the rock characterisation workflow.

2.1. Rock types

Three rocks were chosen due to their distinct depositional features and heterogeneities. The Bentheimer sandstone was deposited in a shallow marine environment and is known for its homogeneity [18]. Its composition was mainly quartz (95%), followed by feldspars (4%) and clays (1%) [19]. Our sample was characterised by a single planar bedding parallel to the principal axis of flow.

The Bunter sandstone is a reservoir sample from a previously proposed CCS site in the Southern North Sea. It is a permeable, porous formation [20], thus was evaluated as a potential storage site for the 2008 CASSEM project (CO_2 Aquifer Storage Site Evaluation and Monitoring project) [21]. The sample exhibited a similar composition to the Bentheimer sandstone, with a majority of quartz and some feldspars and clays [22]. However, this sandstone was more porous and heterogeneous than the former, with distinct layers perpendicular to the principal axis of flow.

The Edwards Brown dolomite represented the most heterogeneous rock we studied. It was quarried from the Upper Cretaceous formation in Texas (USA) [23]. The sample was composed primarily of dolomite and calcite with some quartz [23-24]. The core exhibited isotropic porosity variations with a large ~4cm low-permeable region.

2.2. Core flood experiments

Cylindrical rock samples were plugged with lengths of ~15cm < L < ~20cm and a radius of 1.9cm. Prior to the experiment, the samples were dried in a vacuum. A drainage core-flood was performed on each individual sample in a closed flow loop at constant temperature and pressure. The sample was initially saturated with the wetting fluid (brine or DI water). Chemical equilibrium between the wetting fluid and the rock was ensured by passing several pore volumes of the wetting fluid through the core at high pressure. Thereafter, the core was left saturated for hours. Subsequently, the wetting and non-wetting fluids were co-injected at a constant fractional flow until steady state was reached (stable pressure drop across the core). A medical X-ray CT scanner was then used to image the rock core, thereby measuring the fluid saturations within the sample. The pressure drop across the core was also recorded using pressure transducers. The fractional flow of the non-wetting fluid was increased, and the previous steps were repeated. This continued until the fractional flow of the non-wetting phase reached 1. The fractional flows were chosen to cover a large range of water saturations. The experiment was performed at two flow rates to collect data near the viscous-limit and capillary-limit flow regimes. See Figure 2 for a schematic of the flow loop and Table 1 for a summary of the experimental parameters.

Table 1: Summary of the experimental conditions for the three rock samples.

Experimental Parameters	Bentheimer	Bunter	Edwards Brown
Experimental core length (m)	0.198	0.151	0.148
Experimental core radius (m)	0.019	0.019	0.019
Pressure (MPa)	15.5	13.1	10
Temperature (°C)	50	53	20
Wetting fluid	Deionised Water	Brine	Deionised Water
Non-wetting fluid	Nitrogen	Carbon Dioxide	Nitrogen
Wetting fluid salinity ($molkg^{-1}$)	-	1	-
Total flow rate low ($mlmin^{-1}$)	7	2	0.5
Total flow rate high ($mlmin^{-1}$)	40	20	5
Number of fractional flows high rate	10	8	10
Number of fractional flows low rate	6	6	16

2.3. Core characterisation

Mercury-intrusion porosimetry (MIP) was performed on all the samples to obtain a core-average intrinsic P_c-S_w curve. For the Bentheimer, a sample was taken from the end of the core. For the Bunter and Edwards, sister samples were analysed.

We use a Brooks-Corey model to describe the data, with parameters obtained by minimising the misfit between the MIP data and the model given by Equation 3 [25]:

$$P_c(S_w) = P_e\left(\frac{1 - S_{wirr}}{S_w - S_{wirr}}\right)^{\frac{1}{\lambda}} \quad 3$$

where P_c [Pa] is the capillary pressure as a function of water saturation (S_w [-]), P_e [Pa] is the entry pressure, S_{wirr} [-] is the irreducible water saturation and λ [-] is the pore size distribution factor. A maximum P_c cutoff was applied to the MIP data before fitting. S_{wirr} was determined from the experimental voxel saturations. The values for the parameters from Equation 3 are summarised in Table 2.

The CT images were cropped and coarsened, primarily to reduce the uncertainty in the voxel-scale experimental saturation and speed up the numerical simulations. The amount of coarsening applied to the images was also governed by the REV. It is important to choose a voxel size under which a continuum property has meaning. We verified the REV for porosity by estimating the number of pores present within each voxel using the maximum pore radius obtained from MIP. We recognise that the REV for capillary pressure may be different, however challenging to quantify using the available data. Jackson et al. (2020) and Zahasky et al. (2020) showed that the correlation length scales of capillary pressure and porosity are of a similar order of magnitude. From this, we assumed that capillary pressure is also a valid continuum property at the chosen voxel scale. The image coarsening reduced the standard deviation for the voxel saturation to under 4%. Please refer to [16] for further detail, including a more detailed discussion on REV.

To obtain 3D porosity maps of the rock cores, the CT images were processed using the standard method described in [27]. See Figure 3 for 2D profiles.

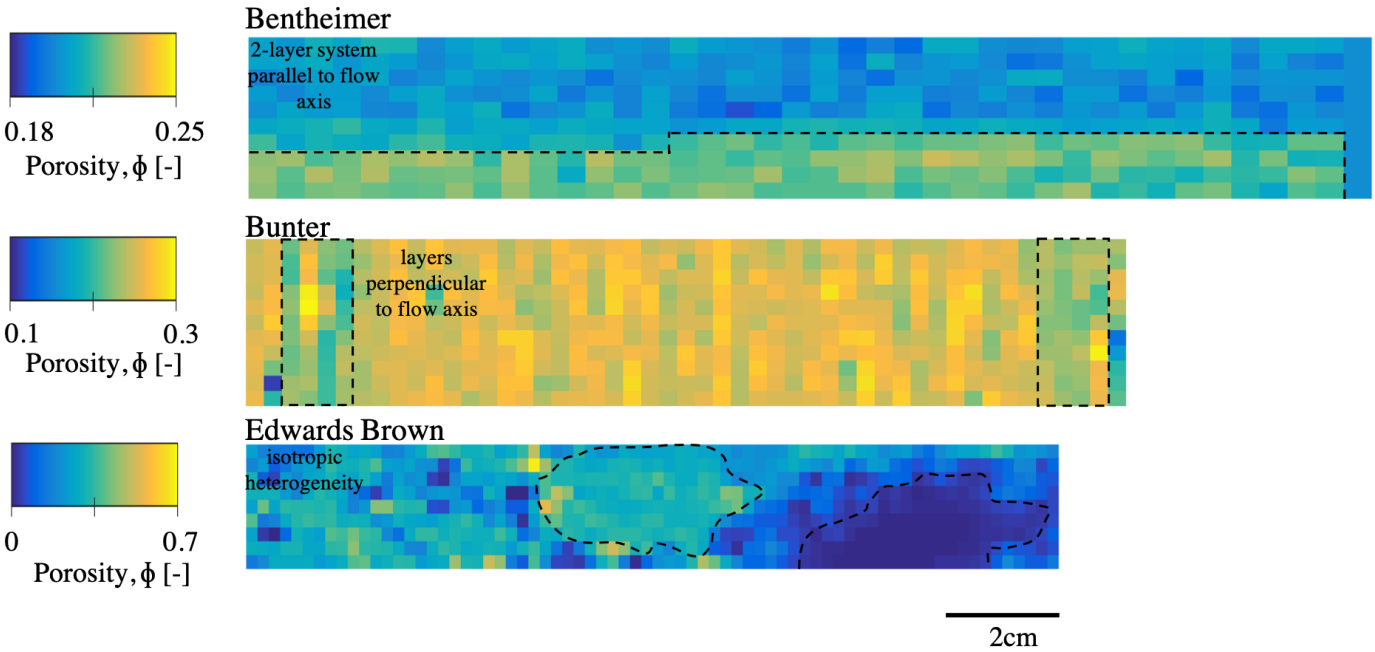

Figure 3: 2D porosity profiles from the central slices for the Bentheimer (top), Bunter (middle) and Edwards Brown (bottom) obtained from the CT images. The key features of each sample are indicated with the black dashed lines. Core dimensions are provided in Table 1.

The core-average pressure drops and saturations recorded at each fractional flow during the high-rate experiment are used to model a viscous-limit, characteristic relative permeability for each sample. This describes the fluid behaviour unaffected by capillary heterogeneity. For the two sandstones, the 1D fluid simulator SENDRA was used to history match the experimental slice average saturation profiles and pressure drops across the core. For the Edwards Brown dolomite, the history match failed to converge to a solution with an acceptable residual error. Hence, Matlab's built-in *fmincon* optimisation tool was used to directly fit the core averaged relative permeability data. In this study, we fitted the relative permeability with the Chierici functional form [28]:

$$k_{rg} = k_{rg}(S_{wirr})e^{-BR_w^m} \quad 4$$

$$k_{rw} = k_{rw}(S_{gc})e^{-AR_w^{-L}} \quad 5$$

$$R_w = \frac{S_w - S_{wirr}}{1 - S_{gc} - S_w} \quad 6$$

where k_{rg} [-] and k_{rw} [-] are the gas and water relative permeabilities, respectively. S_w [-], S_{wirr} [-] and S_{gc} [-] refer to the water saturation, irreducible water saturation and critical gas saturation, respectively. A, B, M and L are the Chierici parameters that control the shape of the curves. The modelling parameters for each sample are summarised in Table 2.

2.4 Characterisation of capillary heterogeneity

To characterise the capillary heterogeneity, we applied the method developed by [14]. The workflow will be briefly described in the following. For further detail, please see [14]. The method is an iterative optimisation scheme, which uses the experimental core flood observations to infer the capillary pressure characteristics within a rock sample. It is an inverse process, which uses the experimental 3D saturation distribution to obtain voxel-scale capillary pressure heterogeneity information. Thus, it was assumed that the capillary heterogeneity can be characterised on a grid block scale. After obtaining an initial guess of the capillary heterogeneity, numerical simulations mimicking the core flood experiment were run to iteratively calibrate the digital model until the residual error reached a certain threshold. Throughout, a mismatch between the simulation and experiment saturations and capillary pressures was assumed to stem from an incorrectly assigned capillary characteristic.

For the initial guess, the capillary pressure within each slice was assumed to be constant and was mapped to the core-average characteristic Brooks-Corey curve obtained in the routine characterisation workflow. A deviation of a voxel-scale saturation from the slice value was assumed to stem from capillary heterogeneity.

Thus, a scaling factor κ was assigned to that voxel, which scales the core-average characteristic curve as the following:

$$P_{c,i}(S_i) = \kappa_i P_{c,avg}(S_i) \quad 7$$

where $P_{c,i}$ is the individual voxel capillary pressure, $P_{c,avg}$ is the average capillary pressure curve, S_i is the experimental voxel saturation and κ_i is the voxel's scaling factor, which represents the capillary heterogeneity. The goal here was to minimise the mismatch between the slice and voxel P_c-S_w values by scaling the capillary pressure curve:

$$\Theta = \sum_{i}^{N_v}\sum_{f}^{N_f}\sqrt{(K_i P_{c,avg}(S_{if}^{exp}) - P_{c,i}(S_{if}^{exp}))^2} \times \sqrt{(S(K_i P_{c,avg}) - S_{if}^{exp})^2} \quad 8$$

where S_{exp} is the experimental voxel saturation, K_i is the individual voxel scaling parameter, N_v is the total number of voxels, N_f is the total number of fractional flows and $S(K_i P_{c,avg})$ represents the saturation of the average capillary pressure curve after it has been scaled (using the slice-average capillary pressure).

Upon completion, a 3D digital model of the sample can be built with this initial guess of the capillary heterogeneity as well as the 3D porosity distribution and the viscous-limited relative permeability, found previously. This is then used in the CMG IMEX fully implicit simulator to simulate the experiment.

Table 2: Summary of experimental and numerical modelling parameters for the three samples

Parameters	Bentheimer	Bunter	Edwards Brown
Experimental core length (m)	0.198	0.151	0.148
Experimental core radius (m)	0.019	0.019	0.019
Entry pressure Pe (kPa)	3.51	1.62	9.18
Pore distribution, λ [-]	2.3	1.43	0.48
Permeability, K_{abs} (D)	1.86	2.20	0.046
Chierici A/L [-]	3/0.75	3/0.9	15.7/1.06
Chierici B/M [-]	5/0.56	3.75/0.4	2.66/0.54
S_{wirr}/S_{gc} [-]	0.08/0.0	0.08/0.0	0.0/0.0
Core-average porosity, ϕ [-]	0.21	0.25	0.23
Coarsened voxel size, $\Delta x, \Delta y$ (m)	0.0032	0.00277	0.00246
Coarsened voxel size Δz (m)	0.005	0.003	0.002

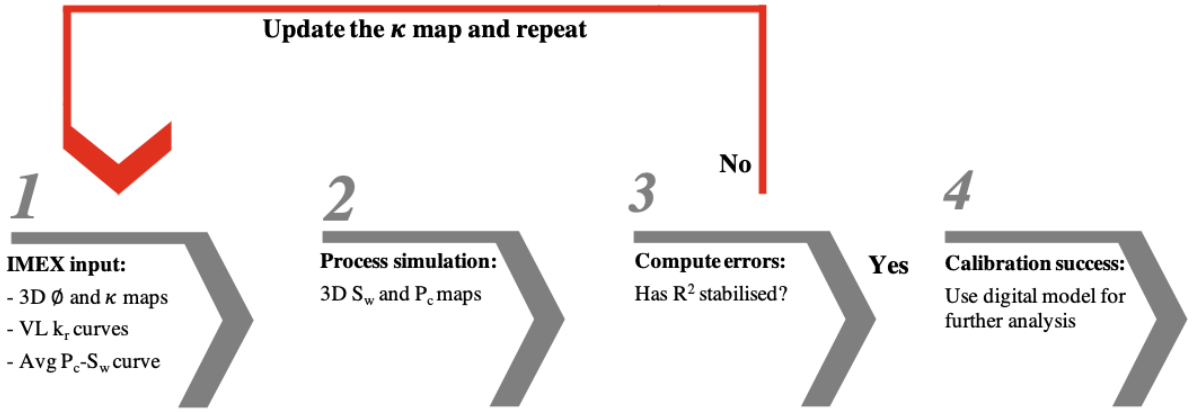

Figure 4: Flow chart summarising the iterative optimisation scheme to characterise the capillary heterogeneity from [14]. VL refers to the viscous limit, high-rate conditions.

A deviation between the experimental and simulation voxel saturations was assumed to stem from an incorrectly assigned κ value. The assumption of constant capillary pressure within each slice was now relaxed. The digital model of the rock core was updated by adjusting the κ values to minimise the following objective function, where S_{if}^{exp} was replaced by S_{if}^{sim}, which represents the voxel-scale simulation saturation:

$$\Theta = \sum_{i}^{N_v}\sum_{f}^{N_f}\sqrt{(K_i P_{c,avg}(S_{if}^{exp}) - P_{c,if}(S_{if}^{sim}))^2} \times \sqrt{(S(K_i P_{c,avg}) - S_{if}^{exp})^2} \qquad 9$$

The optimisation is said to have converged when the error in the voxel saturations, R^2, has stabilised. See [26] for further details. The calibration scheme is summarised graphically in Figure 4.

3. Results and discussion

3.1 Advanced core characterisation

Using the workflow presented in Section 2, the three rock cores were characterised successfully. The success of the models was determined by comparing the voxel saturations and relative permeabilities from the experiment to a core flood simulation. The simulation used the digital, calibrated model and mimicked the core flood performed in the laboratory. The resultant error then provides an indication whether the rock core was adequately characterised using the calibration scheme. See Figure 5 and Table 3 for the resultant errors.

Table 3: Percentage errors of the core-average saturation and pressure drop recorded in the experiment and the core-flood simulation for the three rock samples.

Gas fractional flow	% Error ΔS_w (-)	% Error ΔP(kPa)
Bentheimer		
0.14	4.29	22.16
0.40	0.14	9.75
0.71	5.28	1.81
0.99	10.50	48.58
Bunter		
0.1	6.52	23.87
0.31	12.33	13.53
0.85	4.93	1.19
1.0	5.44	15.92
Edwards		
0.11	2.17	22.77
0.36	0.32	17.57
0.83	1.83	12.17
1.0	3.64	19.44

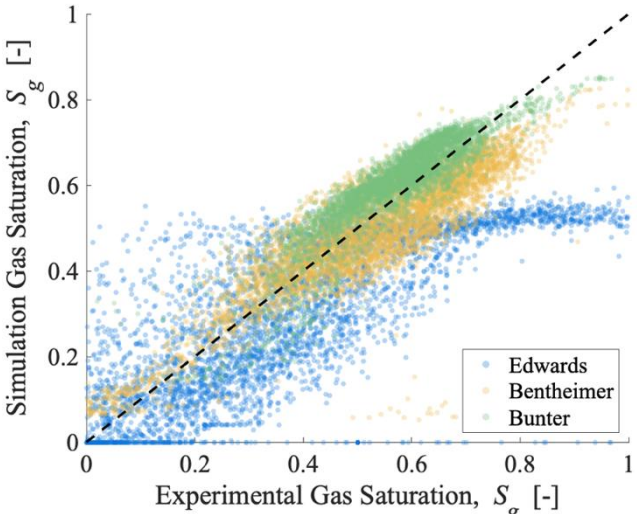

Figure 5: This plot compares the voxel saturation observations from the experiment to the results from the simulation at the final fractional flow. The simulation mimics the core flood experiment using the digital calibrated model. The outliers in the Edwards at high S_g stem from uncertainties in the end effect model in the simulation. These become most prominent at the last fractional flow plotted here.

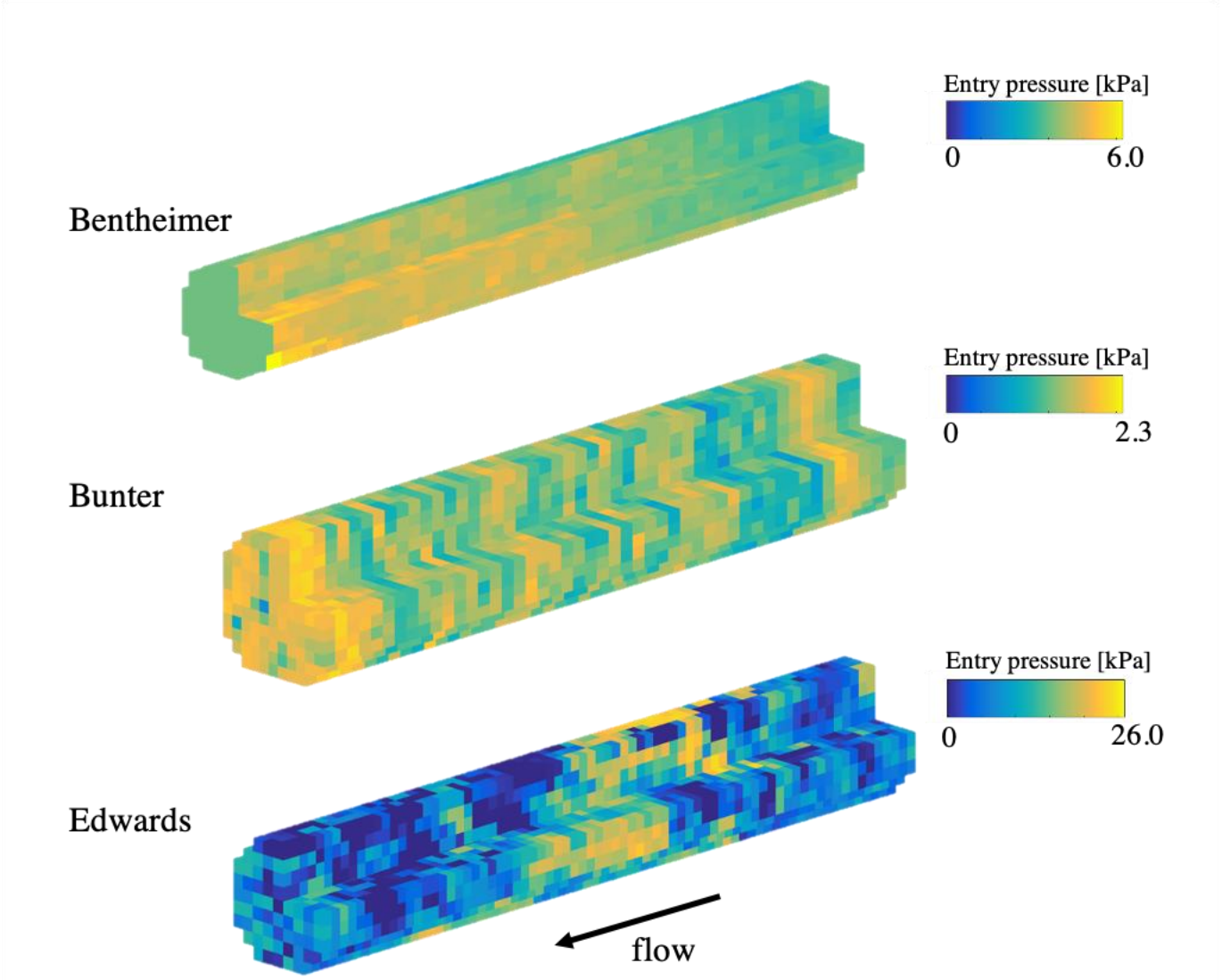

Figure 6: 3D entry pressure maps for the three samples obtained from the workflow described in Section 2.

Pore entry pressure distributions from the final, calibrated models are plotted in Figure 6. As shown, the Edwards Brown has the largest range of entry pressures, followed by the Bentheimer with the Bunter last. The homogeneity of each of the layers in the Bentheimer is clearly visible: each of the two layers displays a relatively uniform entry pressure of 4kPa and 5kPa, respectively. In comparison to this, the perpendicular bedding observed in the porosity map of the Bunter is clearly visible. The entry pressures cluster into distinct layers of low (1kPa) and high (2kPa) regions. Overall, this sandstone sample appears significantly more heterogeneous than the Bentheimer sandstone. Lastly, the Edwards Brown displays the most severe heterogeneity with regions reaching nearly 26kPa. Pressures can be clustered into large vug-shaped regions as was sketched on the 2D porosity profile. The core characterisation workflow has thus allowed us to characterise the spatial distribution of capillary heterogeneity.

3.2 Fluid dynamics

To investigate, in more detail, the varying flow dynamics caused by capillary heterogeneity within each sample, we used the digital models from Section 3.1 to run core flood simulations at varying flow rate. The core-average pressure drops and saturations were used to determine the relative permeability at each rate using Darcy's law, Figure 7. 3D saturation maps were plotted for two of the samples to further illustrate the value these digital models add to our understanding of flow dynamics in heterogeneous rocks (Figures 8 and 9).

From Figure 8 it can be seen that the parallel layering in the Bentheimer sample resulted in capillary cross-flow in the low rate case, enhancing gas flow. After invading the sample, the gas preferentially flows laterally first into the low P_e region, and only then migrates towards the outlet. This resulted in a raised gas relative permeability at high water saturations ($S_w > 0.6$) compared to the viscous-limit curve as the flow rate was lowered, whereas the water relative permeability was reduced (Figure 7, top). At lower water saturations, the end effect is artificially lowering the relative

permeability, see [14] for a detailed discussion. The high-rate simulation results in a homogeneous saturation distribution and thus a lower gas relative permeability.

In comparison to the Bentheimer, the distinct bedding perpendicular to the axis of flow in the Bunter sample hindered fluids from migrating efficiently through the sample. This is observed as a significant reduction of both phase permeabilities with decreasing flow rate (Figure 6, centre).

The Edwards Brown, characterised by isotropic heterogeneity, displays non-monotonic behaviour with increasing rate (Figure 7, bottom). Initially, the relative permeabilities increased with increasing flowrate, after which they decreased again, in agreement with the analytical work by [9]. Referring to the 3D saturation maps from a low-rate simulation ($0.5 ml min^{-1}$) and a high-rate simulation ($100 ml min^{-1}$) shown in Figure 9, it emerges that the isotropic heterogeneity leads to the formation of connected pathway flow, where the gas forms a channel through the low P_e regions in the sample. This results in an increased gas permeability. In contrast to this, the high-rate core flood resulted in a very uniform saturation map, which translates to a lower permeability.

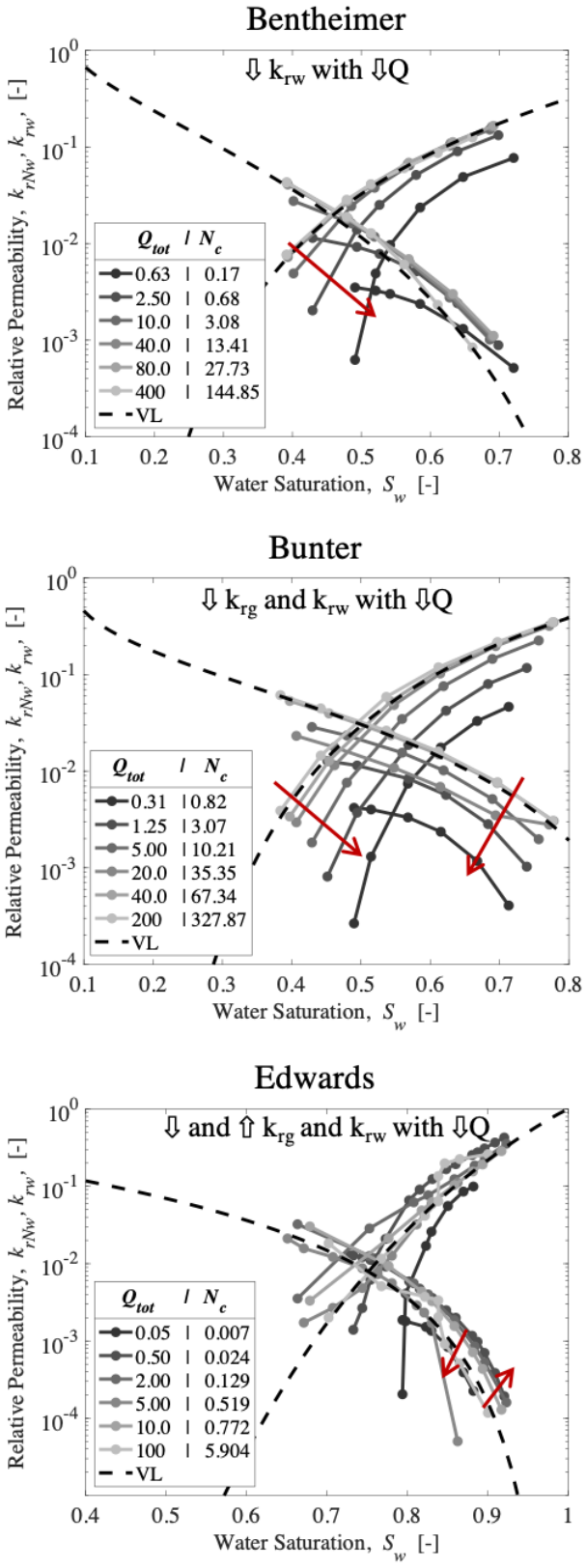

Figure 7: Predicted drainage relative permeabilities at a range of flow rates obtained using the digital models from Figure 6.

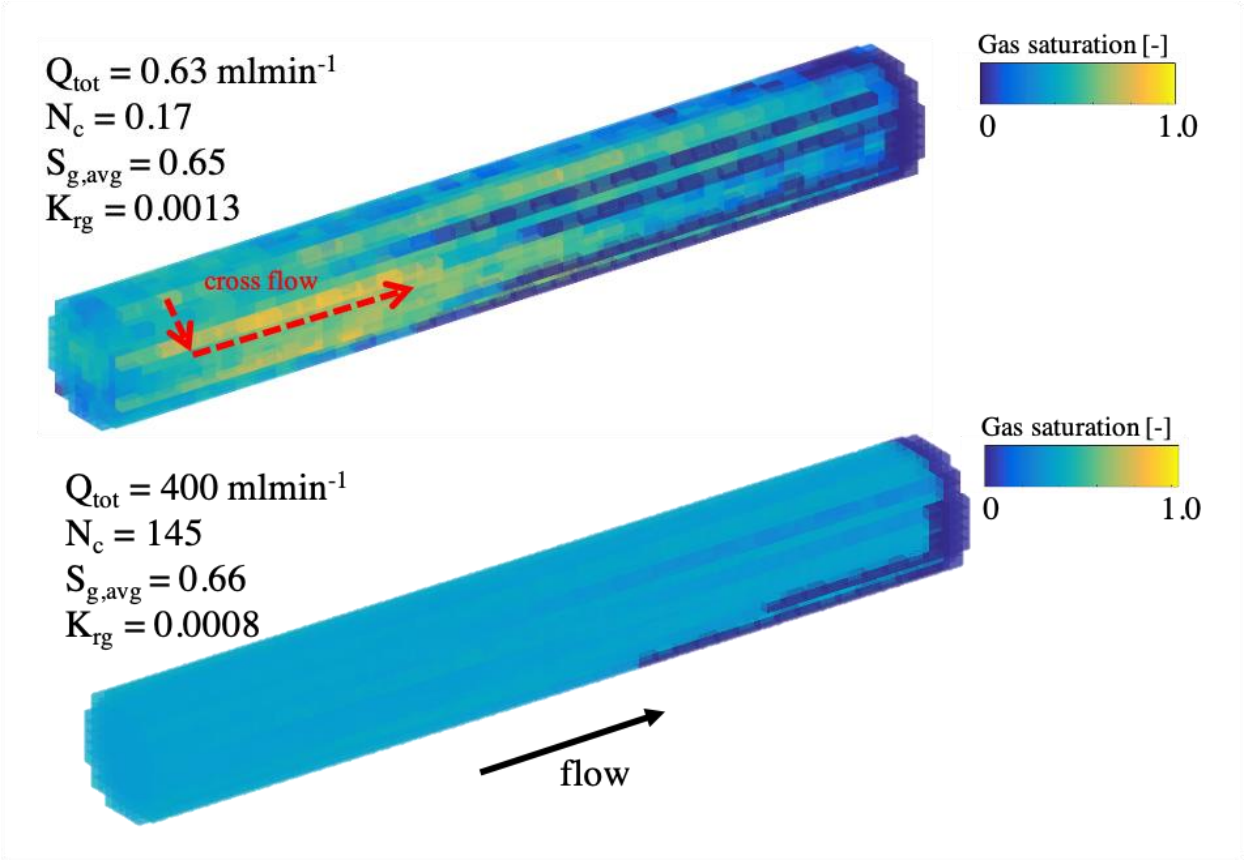

Figure 8: 3D saturation map of the Bentheimer at two distinct simulated flow rates.

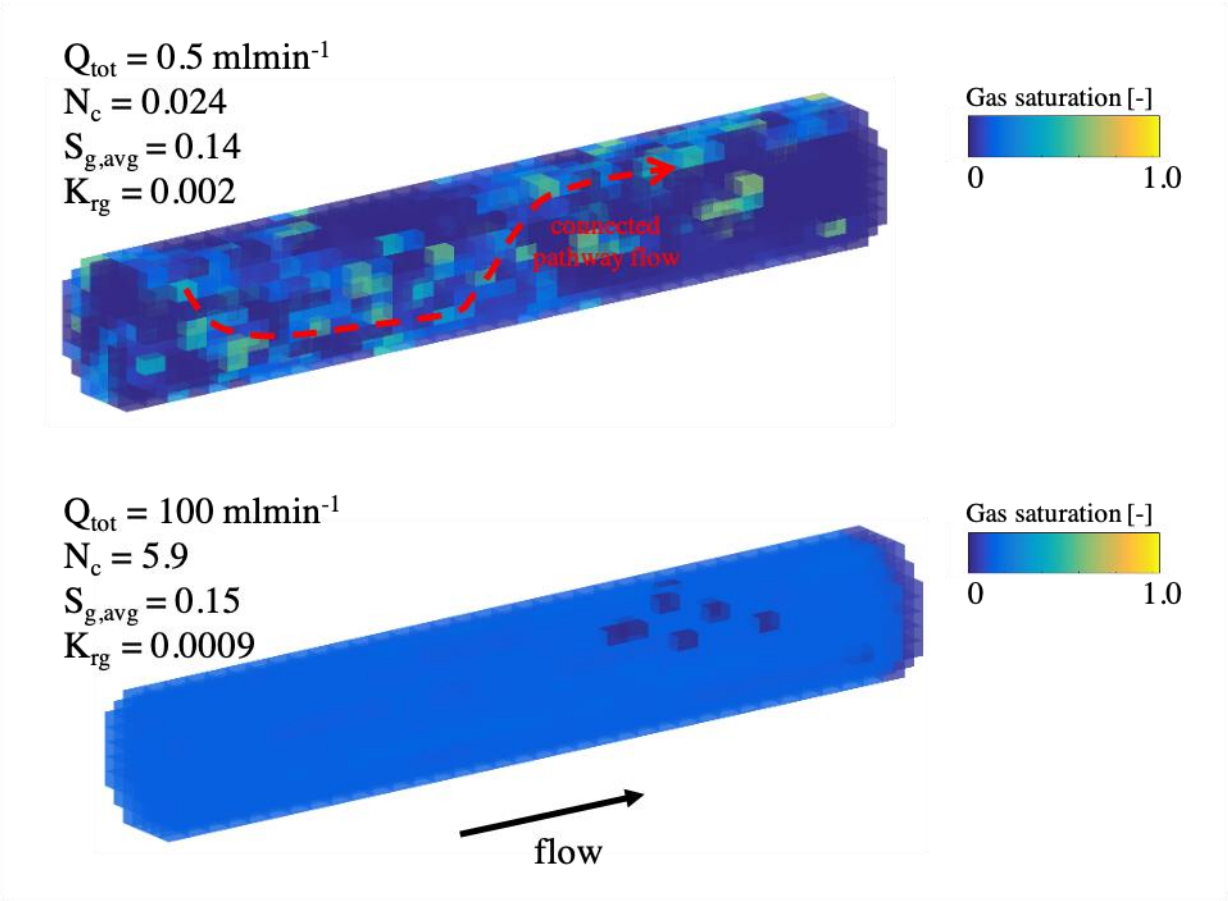

Figure 9: 3D saturation map of the Edwards Brown at two distinct simulated flow rates.

4. Conclusion

We have presented an advanced core characterisation workflow that combines observations from core flood experiments with an iterative numerical optimisation scheme developed by [14]. Three rock samples were selected for this study, two sandstones and one carbonate, with a range of heterogeneity types and length scales. This work represents the first step in an upscaling procedure, whereby the digital models can be used to infer the upscaled impact of capillary heterogeneity at the field scale, as demonstrated in [30].

Drainage core flood experiments were performed on each of the samples [22-23, 29]. A medical X-ray CT scanner was used to image the core saturation and the core-average pressure drops were recorded with pressure transducers. The experiments were performed at two distinct flow rates to obtain multiphase flow parameters in the capillary and viscous flow regimes. After routinely characterising the samples, the experimental core data was used in combination with the optimisation scheme. This was essentially a history match of the core flood experiment, with the voxel-scale saturation distribution as a matching target and the voxel-scale capillary pressure heterogeneity as a fitting parameter. Through this, a 3D digital model of each sample was built incorporating spatial variability in porosity and capillary pressure. The 3D models illustrated the contrasting entry pressure distributions in each sample. The Bentheimer and Bunter sandstones exhibited parallel and perpendicular layering, respectively. The entry pressures in the Edwards Brown were isotropically distributed and could be clustered into large vug-like regions.

Using the digital models, core flood simulations were run at a range of flow rates to investigate the varying flow dynamics in each of the samples. Strong rate dependency of relative permeability was observed in all samples. The parallel layering in the Bentheimer allowed for the phases to cross flow between the layers, which raised the gas relative permeability. In contrast, the Bunter sandstone, with layers orientated perpendicular to the axis of flow, inhibits the flow of both phases, thus the relative permeabilities decreased in the capillary flow regime. Lastly, the Edwards Brown with isotropic heterogeneity exhibited non-monotonic behaviour, where the relative permeability did not display a clear relationship with flowrate. The results illustrate the importance of incorporating rock heterogeneity into flow simulations and the value added from producing these digital models.

5. References

1 M. Muskat, M. Meres, *Phys*., **7**, 9 (1936)
2 M. Muskat, R. Wyckoff, H. Botset, M. Meres, *AIME*, **123**, 1 (1937)
3 H. Welge, *J. Pet. Technol*., **4**, 4 (1952)
4 A. Corey, C. Rathjens, *J. Pet. Technol*., **8**, 12 (1956)
5 T. Kortekaas, *Soc. Pet. Eng. J.,* **25**, 6 (1985)
6 A. Hove, V. Nilsen, *SPE Reserv. Eng*., **5**, 4 (1990)
7 R. Dawe, M. Wheat, M. Bidner, *Transp. in Porous Media*, **7**, 1 (1992)
8 Y. Debbabi, M. Jackson, G. Hampson, P. Salinas, *Transp. in Porous Media*, **124**, 1 (2018)
9 G. Virnovsky, H. Friis, A. Lohne, *Transp. in Porous Media*, **54**, 2 (2004)
10 M. Krause, J. Perrin, M. Benson, (2011), *SPE J.,* **16**, 4 (2011)
11 M. Krause, *SPE Annu. Tech. Conf*. (2012)
12 M. Krause, S. Krevor, S. Benson, *Transp. in Porous Media*, **98**, 3 (2013)
13 M. Krause, S. Benson, *Adv. Water Resour*., **83**, (2015)
14 S. Jackson, S. Agada, C. Reynolds, S. Krevor, *Water Resour. Res.,* **54**, 4 (2018)
15 P. Ringrose, K. Sorbie, P. Corbett, J. Jensen, *J. Pet. Sci. Eng.,* **9**, 2 (1993)
16 S. Hosseinzadeh Hejazi, S. Shah, R. Pini, *Chem. Eng. Sci.,* **200**, (2019)
17 J. Cavanagh, J., B. Nazarian, *Energy Procedia*, **63**, (2014)
18 A. Peksa, K. Wolf, P. Zitha, *Mar. Pet. Geol.,* 67 (2015)
19 M. Andrew, B. Bijeljic, M. Blunt, *Int. J. Greenh. Gas Control*, **22** (2014)
20 M. Stephenson, *Elsevier*. (2018)
21 M. Smith, D. Campbell, E. Mackay, D. Polson, *SCCS*, (2012)
22 C. Reynolds, M. Blunt, S. Krevor, *Water Resour. Res.*, **54**, 2 (2018)
23 S. Manoorkaar, S. Jackson, S. Krevor, *Water Resour. Res.*, **57**, 4 (2021)
24 P. Lai, K. Moulton, S. Krevor, *Chem. Geol.*, **411**, (2015)
25 R. Brooks, A. Corey, *Colorado State University: Hydrology Papers*, **3**,1 (1964)
26 N. Wenck, S. Jackson, A. Muggeridge, S. Krevor, *Water Resour. Res.,* (In review)
27 E. Withjack, *SPE Form. Evaluation*, **3**, 4 (1988)
28 G. Chierici, *SPE J.*, **24**, (1984)
29 C. Reynolds, S. Krevor, *Water Resour. Res.*, **51**, 12 (2015)
30 S. Jackson, S. Krevor, Geophy. Res. Letters, **47**, 18 (2020)